

Coseismic and early postseismic slip models of the 2021 Mw 7.4 Maduo earthquake (western China) estimated by space-based geodetic data

Lijia He^{1,2}, Guangcai Feng^{1,2}, Xiong Xiao Wu^{1,2}, Hao Lu^{1,2}, Wenbin Xu^{1,2}, Yuedong Wang^{1,2}, Jihong Liu^{1,2}, Jun Hu^{1,2}, Zhiwei Li^{1,2}

^a Laboratory of Radar Remote Sensing, School of Geosciences and Info-Physics, Central South University, Changsha 410083, China

^b Key Laboratory of Metallogenic Prediction of Nonferrous Metals and Geological Environment Monitoring, Central South University, Changsha 410083, China

Corresponding author: Guangcai Feng (fredgps@csu.edu.cn)

Keywords: Maduo earthquake; InSAR geodesy; Coseismic slip; Postseismic afterslip.

Key Points

1. Co- and post-seismic deformations and fault-slip distributions of the 2021 Maduo earthquake are derived from space-based geodetic data.
2. A six-segment geological structure model with varied dips and orientations is proposed for the interpretation of the Maduo event.
3. The 1947 Dari earthquake increases the stress in the western rupture zones and partially promotes the fault failure of the Maduo event.

Abstract

The 22th May, 2021 M_w 7.4 Maduo earthquake occurred on an intraplate fault of Bayan-Har block in the Tibet Plateau. Here, we derive the coseismic and early postseismic surface deformations from the Sentinel-1 (S1) interferometric synthetic aperture radar (InSAR) data. We use the subpixel offsets of SAR and Sentinel-2 (S2) optical images to determine the surface rupture traces. The fault geometry and coseismic fault slip distribution of multi-segmented ruptures are estimated by inverting InSAR interferograms and SAR pixel-offsets. We show that at least five fault segments with curved geometry are activated, with a peak coseismic slip of about 5 m. The geodetic data inversion suggests that an NW-striking blind segment near the Eling Lake may have ruptured during the 2021 event. Postseismic slip inversion with the 60-day cumulative line-of-sight (LOS) deformations, shows that the early afterslip of 0.1~0.3 m occurred mostly toward the downdip direction of the main coseismic slip asperities. The afterslip geodetic moment accounts for approximately 15.3% of the coseismic one. Coulomb stress analysis shows that the nucleation of the Maduo earthquake is partially facilitated by the 1947 M 7.7 Dari earthquake.

1. Introduction

The 1600-km-long left-lateral East Kunlun fault (EKF) defines the northern boundary of the Bayan-Har Block, which is one of the most seismically active regions in the Tibetan Plateau, China (Li et al., 2011; Zhu et al., 2021). Over the past century, three destructive earthquakes ($M > 7$) ruptured some segments of the EKF, including the 1937 M 7.5 Huashixia, 1963 M 7.0 Dulan and 2001 M_w 7.8 Kokoxili earthquakes (Fig. 1a), leaving two seismic gaps. One is the Maqin-Maqu seismic gap (Wen et al., 2007), where large earthquakes are expected to occur in the near future. Yet no related sign has been observed. In addition, the EKF is somewhat straight to the west of 98°E but bends ~45° toward the southeast from 98°E to 99.5°E. Across such a fault geometry bending, the slip rate of the EKF decreases from ~10 mm/yr in the west section of 98°E to ~5-6 mm/yr along the Maqin-Maqu segment (Van Der Woerd et al., 1998, 2002; Kirby et al., 2007). Such a slip rate decrement suggests that the deformation is accommodated by some nearby structures and faults. Hence, some faults around the Maqin-Maqu segment, even though the slip rate is low, can be the location of large earthquakes.

On 22th May 2021, an M_w 7.4 earthquake struck the Maduo county of Guoluo prefecture in Qinghai province, western China. This earthquake is another large earthquake ($M > 7$) that occurred

in the Bayan-Har block since the 1947 M7.7 Dari earthquake. Until 30th May 2021, a total of 2979 aftershocks have been recorded by the China earthquake administration (Wang et al., 2021). This event caused severe damages to local buildings and roads, but it did not cause any fatality, fortunately. The moment tensor solutions from teleseismic data and field observations indicate that this event occurred on a nearly E-W trending fault, a secondary fault ~85 km south to the EKF (Pan et al., 2021; Wang et al., 2021). This event occurred within the block, different from most of the large earthquakes ($>M7$) that occurred on the block boundary (including the EKF) during the past 30 years. The rupture fault is ~200 km to the NWW of the Maqin-Maqu seismic gap of the EKF (Fig. 4). The preliminary analysis of seismological data shows that this event is left-lateral strike-slip faulting with a component of normal faulting. However, why did this earthquake not occur on the EKF and how large is the potential seismic hazard of the seismogenic area remain unclear. This earthquake provides a unique chance to understand the seismogenic mechanism and regional seismic hazard risks. After this earthquake, the relocated aftershock sequences (Wang et al., 2021), slip rate across the seismogenic fault (Zhu et al., 2021), the 3D coseismic deformation (Liu et al., 2021) and coseismic source modeling (e.g., Hua et al., 2021; Li et al., 2021; Zhao et al., 2021) are quickly presented, but the complete coseismic deformation from geodetic data and the fault postseismic slip model are seldom reported.

In this study, we first map the coseismic surface deformation fields of the Maduo earthquake using S1 SAR and S2 optical images. We also extract the spatiotemporal evolution of the early postseismic deformation within the first two months using the postseismic InSAR data. Then we estimate the complex fault geometry and coseismic fault-slip of the Maduo earthquake by jointly inverting the intermediate-field InSAR and near-field SAR pixel-offset data. The early postseismic afterslip is also inverted using the 60-day cumulative LOS postseismic deformations. Next, we evaluate both the static stress changes on the seismogenic fault and on the surrounding active faults by the inverted coseismic slip model. We further examine the stress loading associated with the 1947 M7.7 Dari earthquake. Finally, we discuss the interaction between the co- and post-seismic slips, the interpretation of coseismic slip, whether the mainshock activated the NW-striking blind fault and the potential seismic risk of the secondary faults on the EKF.

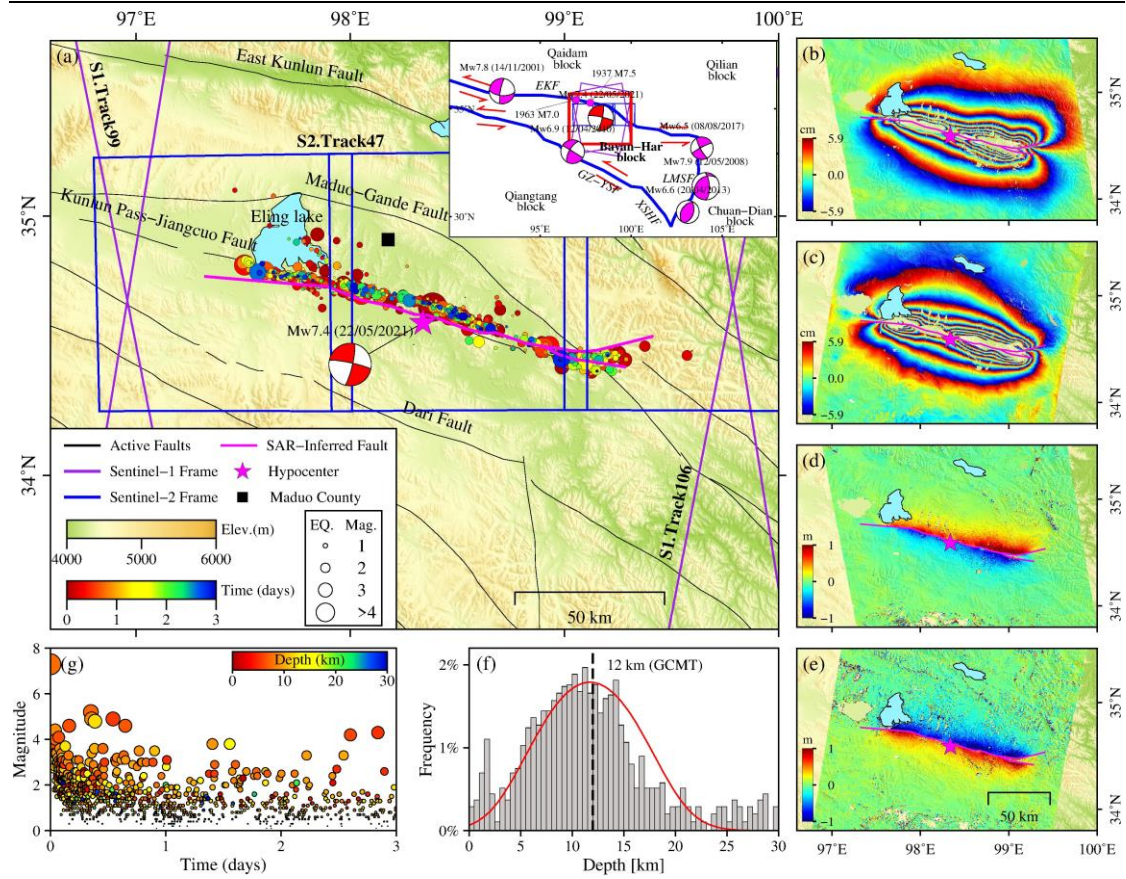


Fig. 1. Overview of the seismogenic area of the 2021 Maduo earthquake on a color-shaded elevation map. (a) Spatial frames of the Sentinel-1 SAR (purple lines) and Sentinel-2 optical (blue lines) data. The complete data coverage is plotted in the upper right inset. The magenta star is the hypocenter location of the mainshock given by CENC. Distribution of relocated aftershocks within the first three days after the mainshock (Wang et al., 2021) is shown as the time-dependent color-coded circles, and the depth frequency of the aftershocks is shown in (f). The magenta lines outline the surface rupture traces inferred from the SAR image offsets in (d) and (e). The upper right inset in (a) shows recent large earthquakes and active faults (blue thick lines) around the Bayan-Har block. The red and magenta beach balls show the epicenter location and focal mechanism of the 2021 Maduo and recent large earthquakes recorded by USGS catalog, respectively. EKF = East Kunlun fault, GZ-YSF = Ganzi-Yushu fault, XSHF = Xianshuihe fault, LMSF = Longmenshan fault. Date in (a) is formatted as day/month/year. (b) and (c) are the InSAR interferograms derived from S1 tracks 99 and 106, respectively. (d) and (e) are the SAR range offsets obtained from S1 ascending and descending images, respectively. (g) shows the magnitude-time evolution of the aftershock sequence by depth-dependent color-coded circles.

2. Data and Method

The detailed image coverage and data information are shown in Fig. 1 and Table S1. We use the differential InSAR (D-InSAR) and the pixel-offset tracking (POT) methods to obtain the line-

of-sight (LOS) displacements and image offsets with the GAMMA software (Werner et al., 2001) (Text S1). To reduce the temporal decorrelation error, we set the coherence threshold as 0.3 and amplitude threshold as 0.3 to eliminate the incoherent pixels located at the vegetation and water regions. To restore the near-field deformation well, image offsets are used in analysis, while the phase measurements are discarded due to the phase unwrapping error caused by the large deformation gradient near the fault traces. To overcome the shortage of polar-orbiting SAR satellites in the north-south direction, we carried out subpixel correlation of the S2 optical images to measure the 2-D horizontal displacement and the location of the surface trace of this event (Text S2).

The detailed surface displacements of this event are presented in Figs. 1 and 2. Both ascending and descending coseismic interferograms exhibit even (close) northern and southern fringe lobes along the whole fault rupture (Figs. 1b, c). This symmetry fringe pattern indicates a near vertical dip angle of the seismogenic fault. The SAR range offset fields maintain observations in the near field (Figs. 1d, e), complementing the data missing in the InSAR phase measurements. The 2-D horizontal coseismic displacement mapped by the optical images shows the E-W and N-S displacement components caused by the left-lateral slip (Figs. 2a, b). Combining the ascending and descending range offsets, we calculate the 2.5-D quasi-E-W and quasi-vertical coseismic displacements (Text S1) (Figs. 2c, d). The results show that the quasi-E-W component becomes larger from the epicentral regions to the eastern and western regions, and the largest horizontal displacements of ~ 2.4 m occurred on the eastern segment of the main fault (at longitude $\sim 98.8^\circ$). Rupture bifurcates at both ends, which has seldom been reported in other earthquakes on the Tibetan Plateau. The quasi-E-W component shows two identifiable lobes, indicating a predominant strike-slip faulting mechanism (Fig. 2c). The quasi-vertical displacement component concentrates near the fault and the magnitude is small (Fig. 2d). We infer that this earthquake is almost a pure left-lateral strike-slip event.

We use the postseismic S1A/B acquisitions at both descending and ascending orbits of the first two months to map the early postseismic deformation by an improved SBAS-InSAR method (Xiong et al., 2020) (Text S1). Thanks to the frequent revisit cycle of S1A/B (6-12 days), we obtain the spatiotemporal evolution of the early postseismic deformations from the 4th day to the 64th day after the mainshock (Fig. S1). The result exhibits that the early postseismic velocity of the InSAR measurement is up to 3 cm/month. Since InSAR is insensitive to the north-south motion, we also derive the 2.5-D quasi-E-W and quasi-vertical postseismic displacement components (Figs. 2e, f). There is no clear vertical displacement along the fault, so the postseismic deformation is dominated by the E-W component that is generally located at the eastern part of the rupture fault.

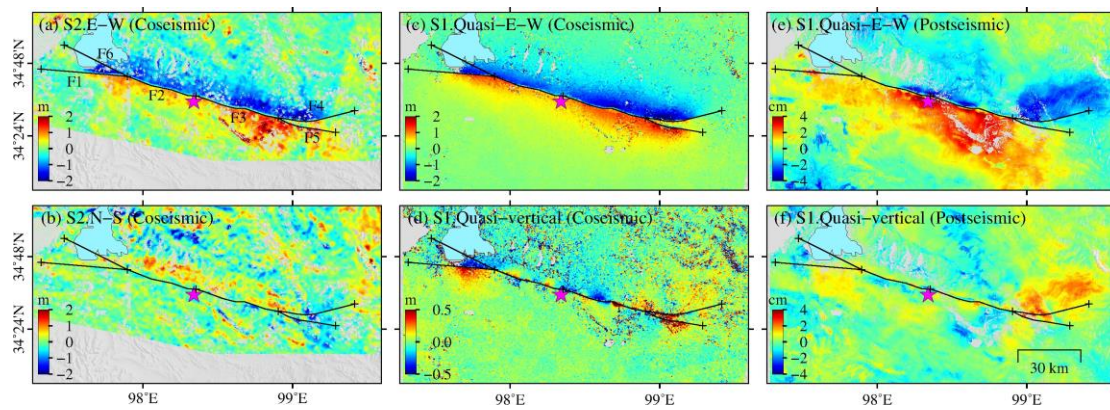


Fig. 2. (a-d) Coseismic and (e-f) postseismic displacement fields of the 2021 Maduo earthquake. (a) and (b) are the east-west and north-south components of the 2-D horizontal coseismic displacement extracted from Sentinel-2 optical data, respectively. (c) and (d) are the 2.5-D quasi-east-west and quasi-vertical coseismic displacement components obtained from the Sentinel-1 SAR pixel-offsets, respectively. (e) and (f) are the 2.5-D quasi-east-west and quasi-vertical postseismic displacement components derived from the 60-day cumulative LOS displacements, respectively. Black lines depict the fault segments F1-F6 used in the linear inversion. The corresponding fault names are labeled in (a). Different color tables are used in (a)-(f).

3. Source Modeling

3.1. Inversion Strategy

Here we utilize a two-step optimization strategy to determine the fault geometry of each segment. Step one, we carry out a non-linear optimization using the genetic algorithm to search for the optimum fault dip, fault width, strike-slip and dip-slip of each segment (named f1-f6, Fig. S3a) that has straight geometry (Text S5). Step two, we adopt a non-straight irregular fault trace to each segment (named F1-F6, Fig. S3b) to fit the InSAR-derived surface coseismic displacements. We discretize the fault planes into non-planar triangular sub-patches to estimate a more detailed fault-slip distribution. We use a 3-D finite element mesh-generation software (Geuzaine & Remacle, 2009) to construct triangular meshes (Text S6). Compared with the rectangular dislocation elements, the triangular elements are more suitable for source modeling of the more complex and curved fault geometries that have no sub-patches overlapping. On the basis of the InSAR interferograms and SAR pixel-offsets, we invert the coseismic slip using the fast non-negative constrained least square algorithm (Bro & Jong, 1997). On the basis of the 60-day cumulative postseismic LOS deformations, we also invert the early postseismic slip using the same fault geometry and inversion scheme as that of the coseismic slip inversion. Differently, the Bounded Variable Least Squares algorithm is used to solve the linear problem in inverting the afterslip distribution (Stark & Parker, 1995).

We calculate the Coulomb Failure Stress change (Δ CFS) of the surrounding faults induced by the 1947 Dari and 2021 Maduo earthquakes (Text S9). On the basis of the empirical relationships of historic seismicity inferred by Wells & Coppersmith (1994), we estimate the average displacement (4.1 m), surface rupture length (141 km) and downdip width (21 km) of the 1947 M7.7 Dari event. Then we calculate the stress using friction coefficients of 0.2, 0.4 and 0.6 (Figs. S13a-c). Although the elastic stress interaction exerted by coseismic rupture is important, the viscoelastic stress interaction arising from some large historical earthquakes (e.g., the 1937 Huashixia, 1947 Dari and 1963 Dulan earthquakes; Fig. 1a) is non-negligible in some cases (e.g., Liu et al., 2015, 2021). Here, we do not calculate them, because the spatiotemporal deformation gradients of these events may be modest across the region.

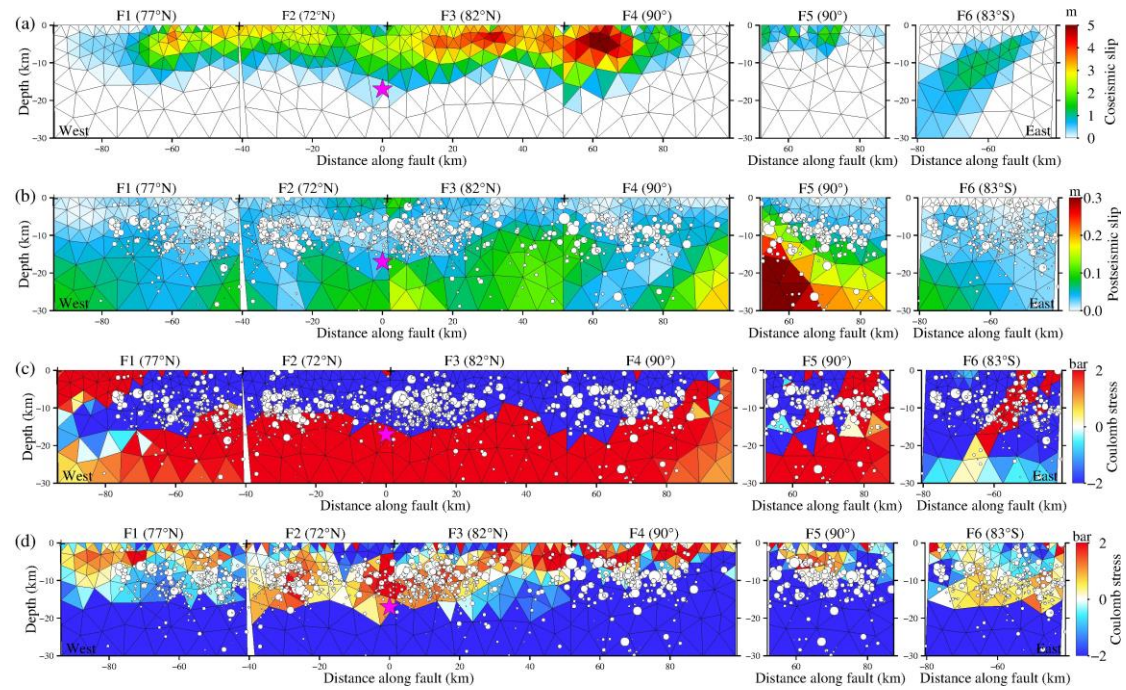


Fig. 3. (a) Coseismic and (b) postseismic slip distributions of the 2021 Maduo earthquake. (c) Coulomb stress changes on the six fault segments calculated by the five-segment coseismic slip shown in Fig. S11a. (d) Coulomb stress changes induced by the postseismic afterslip. Aftershock sequence of the first nine days after the mainshock (Wang et al., 2021) overlays on the stress results. Different color tables are used in (a)-(d).

3.2. Inversion Results

Figure 3a shows the coseismic slip distribution of the best-fitting six-segment slip model. The fault segments F1-F3 from west to east dip 77° , 72° and 82° toward the north, respectively, while the eastern segments F4-F5 dip vertically. The NW-striking blind segment F6 dips 83° toward the south. The majority of fault slip concentrates between 0 km and 20 km, with a maximum slip of ~ 5

m on segment F4 at a shallow depth of ~6 km. There are also moderate slips along other fault segments, for example, a slip of ~3 m on segments F1-F2, a ~4 m slip on segment F3 and a ~2 m slip on segment F5. The slip on segments F1-F5 reaches the surface. This is in agreement with the geological surface offset measurements (Pan et al., 2021). This earthquake was dominated by left-lateral strike-slip motions and accompanied with minor normal component near the surface. The best-fitting model restored the coseismic deformation fields well (Fig. S10). The geodetic moment and magnitude released by each fault segment are listed in Table S4. The total geodetic moment released by the coseismic slip is approximately 1.58×10^{20} N·m, corresponding to a moment magnitude of an $M_w 7.43$ earthquake.

As shown in Fig. 3b, the postseismic afterslip has a magnitude of 0.1~0.2 m on segments F1, F2 and F4. The afterslip mainly occurs in the downdip direction of the coseismic slip zones, with the peak magnitude of about 0.3 m on segment F5 at a depth of 10~30 km. A few afterslip (~ 0.05 m) is found on segment F6. The postseismic afterslip motion is dominated by left-lateral strike-slip, which is in agreement with the slip characteristic of the coseismic slip. The predicted postseismic deformations and residuals are shown in Fig. S11. The afterslip model can reproduce most of the near-field observed deformation. The total geodetic moment released by the 60-day afterslip is about 2.42×10^{19} N·m (Table S4), corresponding to that of an $M_w 6.89$ earthquake, and accounts for about 15.3% of the coseismic geodetic moment.

4. Discussion

4.1. Comparison of Coseismic Slip Models

We compare the coseismic slip model of the 2021 Maduo earthquake with three representative models using both seismic and geodetic data (Hua et al., 2021; Li et al., 2021; USGS, 2021) in terms of fault geometry, slip magnitude and distribution. For the fault geometry, Hua et al. (2021) constructed a curved fault model with a constant dip optimized by InSAR data, but they neither considered the dip complexity along the fault nor the branch segments at both ends of the main fault in source modeling. Li et al. (2021) and USGS (2021) used a simplified fault model with single strike and dip angles. The coseismic slip model of the former was constrained by the GPS measurements and the latter by the seismological waveforms. In this study, on the basis of the InSAR interferograms and SAR pixel-offsets, we employ a six-segment fault model with variable strike and dip angles. To quantitatively evaluate the effects of the dip on the inversion result, multiple sets of inversions are performed by varying the dip of each segment from 60° northward-dipping to 60° southward-dipping. We also test the slip difference between the five- and six-segment models to

investigate whether the NW-striking blind fault near the Eling Lake (at longitude $\sim 97.8^\circ\text{E}$, Fig. 1a) is activated during this earthquake.

For slip magnitude, the maximum slip of the models of Hua et al. (2021) and Li et al. (2021) are 4-5 m near the eastern end of the main fault, while it is ~ 3.2 m in the model of USGS (2021). In addition, the slip distribution obtained by these models is different. The model of Li et al. (2021) has two asperities, but other models have at least two more asperities. The locations are also different in different models. The slip distribution in the model of Hua et al. (2021) is more concentrated than that of Li et al. (2021) and USGS (2021) models, who used the data with higher spatial density. These comparisons are not to determine which model is better, because many factors could influence the inversion results, such as simplified fault geometry, discretization and parameterization of modeled fault, kinematic assumption, selection of data, smoothing factor and dislocation theory (e.g., half space and earth spherical models). Although these factors would lead to different inversion results and data fittings, from which we can get some insights on the understanding of the uncertainty of different model inversions. We hope that these comparisons can help to evaluate the contribution of source modeling for understanding the static rupture process of the Maduo earthquake.

4.2. Interplay between the Co- and Post-seismic Slips

Aseismic afterslip, viscoelastic relaxation and poroelastic rebound are the three main mechanisms responsible for postseismic transients (e.g., Liu et al., 2021). Many studies have attributed the early postseismic deformation spanning from several days to months to afterslip (e.g., Sreejith et al., 2016; Liu & Xu, 2019). Our spatiotemporal postseismic deformation patterns suggest that some extensive aseismic slips reach the surface and surround the rupture (Figs. 3b and S1), so the aseismic afterslip is the most likely driving process causing the short-term postseismic transient motion.

From the comparison between the coseismic and postseismic slips along the causative fault, we find that the postseismic slip mainly occurs toward the down-dip direction of the coseismic slip asperities (Figs. 3a, b), suggesting a complementary relationship between them. If we consider the rate-and-state friction, the aseismic afterslip distribution can be related to the frictional properties of a rate-strengthening (RS) material (Scholz, 1998; Dianala et al., 2020). RS materials are expected at depth to provide physical conditions for aseismic afterslip, but there might also be places more strengthening than other at a shallow depth. Aseismic afterslip is also expected along the seismogenic portion of strike-slip faults. In addition, some minor afterslip patches in the shallow

depth of segments F2 and F3 overlap the coseismic slip asperities. One reason is the response of shallow fault to stress reorganization and/or shallow material redistribution. Another reason is that the postseismic afterslip likely occurs before the acquisition of the first postseismic SAR image on 26th May 2021. The complementary relationship between the coseismic slip and postseismic afterslip of this event can also be found in other tectonic environments, such as the 2001 M_w 7.8 Kokoxili (Wen et al., 2012) and 2010 M_w 6.9 Yushu (Zhang et al., 2016) earthquakes, where the afterslip distributed randomly along the up-dip and down-dip directions of the main coseismic ruptures. But in the 2004 M_w 6.0 Parkfield strike-slip earthquake (Johnson et al., 2006), the afterslip primarily occurred in the up-dip region of the coseismic rupture.

Comparison between the postseismic afterslip and Coulomb stress change indicates that the majority of afterslip is triggered in the regions with positive coseismic stress changes (~ 2 bar) (Figs. 3b, c), suggesting the Maduo event generates a stress-driven afterslip. This result is in agreement with the physics-based assumption of stress-driven afterslip model, in which the increased stress driven by coseismic slip should be subsequently released aseismically (Johnson et al., 2006). Although aftershocks are expected to be stress-driven, most aftershocks falls in a region with CFS decreased induced by the coseismic slip (Fig. 3c). The possible explanations include: (1) poorly determined depth of the aftershocks, (2) aftershocks are not on the main fault plane but in the bulk, (3) afterslip drives the distribution of aftershocks (i.e., the CFS change induced by the afterslip drives the distribution of aftershocks, Fig. 3d), (4) unresolved complexity along the main rupture and (5) the coseismic slip distribution might be too smooth and aftershocks appear in a low CFS region.

4.3. Interpretation of Coseismic Slip

In the eastern triple junction where the main rupture splits into two fault branches F4 and F5, slip increases progressively eastward from segment F3 (~ 4 m) to F4 (~ 5 m), and drop abruptly on F5 to ~ 2 m. The rupture tends to follow F4, a segment whose strike is $\sim 20^\circ$ from the main rupture (F2-F3), rather than along F5, a segment whose strike follows the main rupture. A similar signature associated with branch faults connecting to the rupturing fault has also been suggested for the 2001 M_w 7.8 Kokoxili earthquake, and was interpreted as the transition between slipping segment and geometric barrier (Klinger et al., 2006). A tough barrier may form between the eastern termination of segment F3 and the western part of F5, which may impede the rupture propagation along F5 and force the rupture to transfer to F4. In addition, within the first six hours after the mainshock, a large cluster of aftershocks occur along F4, and a smaller cluster of aftershocks occur

along F5 (Fig. S14). In the next few days, more aftershocks occur along F5, but the total number is still significantly less than that along F4. This confirms that the rupture tends to propagate along F4 more than F5.

There are several residuals cannot be explained by the inverted coseismic slip model. In the south area of segment F1, all the data fittings consistently show few residuals (Figs. S10d, S11d). This residual pattern does not rely on the coseismic slip parameters, but could be associated with an additional seismogenic structure that we do not consider in source modeling. The eastern section of the Kunlun Pass-Jiangcuo fault, close to segment F1, somewhat overlaps in space with the aftershock sequence within the first three days after the mainshock (Fig. 1a). We infer that this fault may have been reactivated during the Maduo event, resulting in high post-earthquake seismicity and yielding surface deformation that cannot be recovered by the coseismic slip. Future long-term InSAR time-series analysis and precise postseismic focal mechanisms estimation will help us to further verify these inferences. In addition, in the south area of segment F5, the descending LOS coseismic displacement is not well reproduced by the coseismic slip model (Fig. S11d). This is because a part of the slip component on F5 may be mapped into F4 during the linear inversion, resulting in a loss of slip on F5.

4.4. Whether the NW-striking Branch Fault was Activated

The inversion result of the six-segment model shows that the maximum slip of ~1.5 m occurs on the NW-striking segment F6 (Fig. 3a). This branch fault is not only a blind fault (Pan et al., 2021), but also is consistent with a linear distribution of the aftershock relocation (Wang et al., 2021). To investigate whether it was activated during the 2021 Maduo earthquake, we construct a five-segment fault model to invert the fault-slip. We find that the coseismic fault-slip distribution on segments F1-F5 and data prediction of the optimal six- and five-segment models are similar (Figs. S10c and S11c), but the data RMS misfit of the formal model (72.8 mm) is slightly smaller than the latter one (77.6 mm). The insignificant difference in data misfit is not sufficient to answer the question.

In order to further test the six-segment model, we compare the Sentinel-1 ascending LOS displacement residuals of the five- and the six-segment coseismic slip models. As the black dashed box in Fig. S10d shows, there is a tiny lobe in the residual map, which cannot be fitted by the five-segment model. But in Fig. S11d, there is no significant fringe in the residual map of the six-segment model. Combining the field investigation, data misfit comparison and the difference in data fitting residuals, we suggest that the NW-striking branch fault segment F6 is likely to be activated by the Maduo event.

4.5. Potential Seismic Risks on the Secondary Faults of the EKF

The 2021 Maduo earthquake occurred on a secondary fault (Kunlun Pass-Jiangcuo fault), not on the EKF of the Bayan-Har block where extensive deformations are observed and three $M > 7$ earthquakes occurred (Fig. 1a). The seismic gap of the main boundary zones, such as the Maqin-Maqu segment of the EKF had drawn much attentions and got a lot of comprehensive studies (Diao et al., 2019; Zhu et al., 2021). But most secondary faults inside the Bayan-Har block have been ignored, due to their slow strain accumulation from geodetic slip rate (Wang et al., 2007). There are a series of parallel secondary faults with a left-lateral strike-slip mechanism between the north and south boundaries of the Bayan-Har block, such as the Kunlun Pass-Jiangcuo, Maduo-Gande, Dari and Bayan-Har Mountain faults (Fig. 4). In addition, an $M 7.7$ Dari earthquake happened on the nearby Dari fault in 1947 (Liang et al., 2020), with the seismic mechanism and magnitude similar to the 2021 Maduo event. Furthermore, some recent earthquakes ($M > 5$) occurred at those secondary faults, especially at the Dari and Maduo-Gande faults (Fig.4). Therefore, the seismic risk of those secondary faults of the EKF was seriously underestimated.

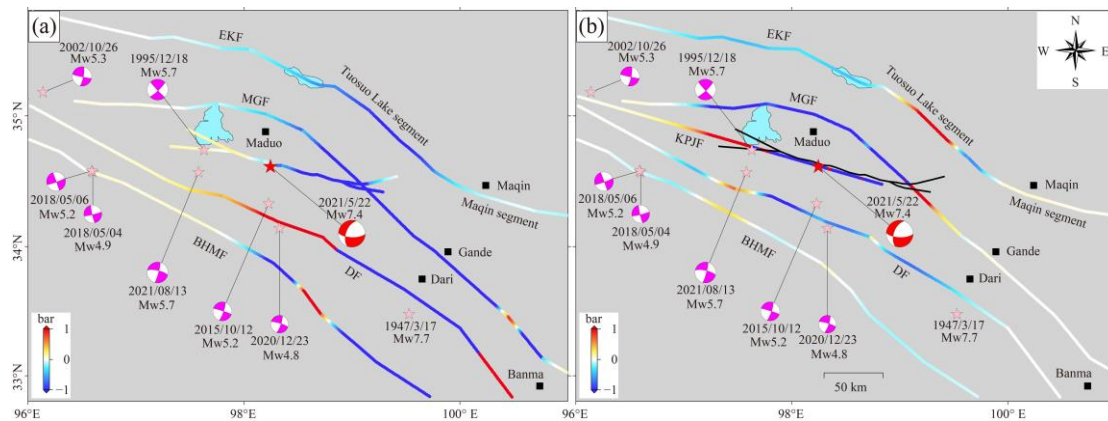


Fig. 4. Static Coulomb stress changes induced by (a) the 1947 Dari and (b) the 2021 Maduo earthquakes using a friction coefficient of 0.4. The focal mechanism of the red beach balls is recorded by the USGS catalog. EKF = East Kunlun fault, MGF = Maduo-Gande fault, KPJF = Kunlun Pass-Jiangcuo fault, DF = Dari fault, BHMF = Bayan-Har Mountain fault. Dates are formatted as year/month/day.

The small geodetic slip rates are one of the main reasons of the underestimated seismic risks on those secondary faults. Using dense near-field GPS observation profiles across the Kunlun fault, Zhu & Diao et al. (2021) inverted the slip rate of 1.2 ± 0.8 mm/yr on the seismogenic fault. The similar slip rate also had been inverted using the interseismic deformations derived from the S1A/B InSAR data during 2014-2019 (Zhu & Ji et al., 2021). Both the geodetic and geological studies reported that the slip rates dramatically decrease from 10-15 mm/yr in the western to 2-8 mm/yr in the eastern sections of the Kunlun fault (Van Der Woerd et al., 1998, 2002; Kirby et al., 2007; Wang & Shen, 2020). There were several kinds of explanations for the slip rate variation (Kirby et al.,

2007; Li et al., 2011; Diao et al., 2019), but we infer that the parallel secondary faults between the north and south Bayan-Har block also have absorbed the strain together with the main fault. The occurrences of the 1947 Dari, 2021 Maduo earthquakes and a series of $M > 5$ events over the past century provide direct evidence for the strain accumulation. Nevertheless, how much strain has been released and whether it is the main reason of the slip rate decrease need further investigation using more geodetic observations surrounding the faults.

For a better understanding of the stress change and seismic risk on those secondary faults, we analyze the role of the 1947 Dari event played in the fault failure of the 2021 Maduo event. The 1947 event has yielded positive ΔCFS of ~ 0.4 bar in the west rupture zones of the 2021 event and a neutral ΔCFS in the epicentral region (Fig. 4a). The effect of the 2021 event on the regional stress field is also calculated. The result indicates that the ΔCFS on the western Dari fault, the Tuosuo Lake and Maqin segments are enhanced by this event (Fig. 4b), which increases the seismic hazard risks in those regions. The largest aftershock with the moment magnitude of 5.7 occurred on 13th August 2021 is also located at a ΔCFS enhanced area (Fig. 4b). So we should pay more attention to those secondary faults that have not experienced any documented $M > 6$ earthquakes, such as the Bayan-Har Mountain and eastern Maduo-Gande faults. Future seismic hazard assessments on these faults are required.

5. Conclusions

In this study, we use the intermediate-field InSAR and near-field SAR pixel-offset data to constrain the fault geometry and coseismic slip distribution of the 2021 Maduo earthquake. The inversion results suggest that at least five fault segments ruptured, with varied dips and orientations. The geodetic inversion shows that there is a tiny lobe in the residuals that cannot be explained by the five-segment model, justifying the need for the sixth fault segment near the Eling Lake. We also estimate the early postseismic afterslip using the cumulative LOS deformations in the first two months following the earthquake, and find a complementary relationship between the coseismic slip and postseismic afterslip. The geodetic moment released by the afterslip is about 2.42×10^{19} N·m, which is equivalent to that of an $M_w 6.89$, and accounts for about 15.3% of the coseismic geodetic moment (1.58×10^{20} N·m, $M_w 7.43$). The stress analysis suggests that the 1947 $M 7.7$ Dari earthquake has partially promoted the rupture failure of the 2021 Maduo earthquake through positive stress loading (~ 0.4 bar) in the western rupture zones. Moreover, some regions have increased ΔCFS induced by the Maduo event, so further attention should be paid to the potential seismic hazard risks associated with the Bayan-Har Mountain and eastern Maduo-Gande faults, the

Acknowledgments

The authors thank the editor Lucy Flesch, Romain Jolivet and an anonymous reviewer for their thoughtful and constructive comments that greatly improved this manuscript. This work was supported by the National Key R&D Program of China (No. 2018YFC15036003), the Innovation-Driven Projects of Central South University (No. 2019CX007), and the Innovation Foundation for Postgraduate of Central South University (No. 2021zzts0250). The Figures in this study were generated by the Generic Mapping Tools (Wessel et al., 2013). We thank the COSI-Corr open source software for optical data processing (<http://www.tectonics.caltech.edu>).

Data Availability Statement

The Sentinel-1 SAR data and Sentinel-2 optical data used in this study are copyrighted by the European Space Agency (<http://scihub.copernicus.eu/dhus>) and additionally distributed by the Alaska Satellite Facility Distributed Active Archive Center (<https://vertex.daac.asf.alaska.edu>). The aftershock sequence catalog is publicly available at the website of the China Seismic Array Data Management Center (<http://www.chinarraydmc.cn/highlights/queryPage?mid=44&mpid=28>).

References

- Bro, R., & De Jong, S. (1997). A fast non-negativity-constrained least squares algorithm. *Journal of Chemometrics: A Journal of the Chemometrics Society*, 11(5), 393-401. [https://doi.org/10.1002/\(SICI\)1099-128X\(199709/10\)11:5<393::AID-CEM483>3.0.CO;2-L](https://doi.org/10.1002/(SICI)1099-128X(199709/10)11:5<393::AID-CEM483>3.0.CO;2-L).
- Diao, F., Xiong, X., Wang, R., Walter, T. R., Wang, Y., & Wang, K. (2019). Slip rate variation along the Kunlun Fault (Tibet): Results from new GPS observations and a viscoelastic earthquake - cycle deformation model. *Geophysical Research Letters*, 46(5), 2524-2533. <https://doi.org/10.1029/2019GL081940>.
- Dianala, J. D. B., Jolivet, R., Thomas, M. Y., Fukushima, Y., Parsons, B., & Walker, R. (2020). The relationship between seismic and aseismic slip on the Philippine Fault on Leyte Island: Bayesian modeling of fault slip and geothermal subsidence. *Journal of Geophysical Research: Solid Earth*, 125(12), e2020JB020052. <https://doi.org/10.1029/2020JB020052>.
- Geuzaine, C., & Remacle, J. F. (2009). Gmsh: A 3-D finite element mesh generator with built-in pre-and post-processing facilities. *International journal for numerical methods in engineering*, 79(11), 1309-1331. <https://doi.org/10.1002/nme.2579>.
- He, L., Feng, G., Li, Z., Feng, Z., Gao, H., & Wu, X. (2019). Source parameters and slip distribution of the 2018 Mw 7.5 Palu, Indonesia earthquake estimated from space-based geodesy. *Tectonophysics*, 772, 228216.

<https://doi.org/10.1016/j.tecto.2019.228216>.

- Hua, J., Zhao, D., & Shan, X. (2021). Coseismic deformation field, slip distribution and Coulomb stress disturbance of the 2021 Mw 7.3 Maduo earthquake using sentinel-1 InSAR observations [J]. *Seismology and Geology*, 43(3): 677—691. <https://doi.org/10.3969/j.issn.0253-4967.2021.03.013>.
- Johnson, K. M., Burgmann, R., & Larson, K. (2006). Frictional properties on the San Andreas fault near Parkfield, California, inferred from models of afterslip following the 2004 earthquake. *Bulletin of the Seismological Society of America*, 96(4B), S321-S338. <https://doi.org/10.1785/0120050808>.
- Kirby, E., Harkins, N., Wang, E., Shi, X., Fan, C., & Burbank, D. (2007). Slip rate gradients along the eastern Kunlun fault. *Tectonics*, 26(2). <https://doi.org/10.1029/2006TC002033>.
- Leprince, S., Barbot, S., Ayoub, F., & Avouac, J. P. (2007). Automatic and precise orthorectification, coregistration, and subpixel correlation of satellite images, application to ground deformation measurements. *IEEE Transactions on Geoscience and Remote Sensing*, 45(6), 1529-1558. <https://doi.org/10.1109/tgrs.2006.888937>.
- Li, C., Xu, X., Wen, X., Zheng, R., Chen, G., Yang, H., ... & Gao, X. (2011). Rupture segmentation and slip partitioning of the mid-eastern part of the Kunlun Fault, north Tibetan Plateau. *Science China Earth Sciences*, 54(11), 1730. <https://doi.org/10.1007/s11430-011-4239-5>.
- Liu, S., Shen, Z. K., & Bürgmann, R. (2015). Recovery of secular deformation field of Mojave Shear Zone in Southern California from historical terrestrial and GPS measurements. *Journal of Geophysical Research: Solid Earth*, 120(5), 3965-3990. <https://doi.org/10.1002/2015JB011941>.
- Liu, X., & Xu, W. (2019). Logarithmic model joint inversion method for coseismic and postseismic slip: Application to the 2017 Mw 7.3 Sarpol Zahāb earthquake, Iran. *Journal of Geophysical Research: Solid Earth*, 124(11), 12034-12052. <https://doi.org/10.1029/2019JB017953>.
- Liu, S., Shen, Z. K., Bürgmann, R., & Jónsson, S. (2021). Thin crème brûlée rheological structure for the Eastern California Shear Zone. *Geology*, 49(2), 216-221. <https://doi.org/10.1130/G47729.1>.
- Liang, M. J., Yang, Y., Du, F., Gong, Y., Sun, W., Zhao, M., & He, Q. (2020). Late quaternary activity of the central segment of the Dari fault and restudy of the surface rupture zone of the 1947 M7 3/4 Dari earthquake, Qinghai province. *Seismology and Geology*, 703-714. <https://doi.org/CNKI:SUN:DZDZ.0.2020-03-011>.
- Li, Z. C., Ding, K. H., & Zhang, P. (2021). Co-seismic deformation and slip distribution of 2021 Mw 7.4 Maduo earthquake from GNSS observation. *Geomatics and Information Science of Wuhan University*, 1-10. <https://doi.org/10.13203/j.whugis20210301>.
- Liu, J., Hu, J., Li, Z., Ma, Z., Wu, L., Jiang, W., ... & Zhu, J. (2021). Complete three-dimensional coseismic displacements due to the 2021 Maduo earthquake in Qinghai Province, China from Sentinel-1 and ALOS-2 SAR images. <https://doi.org/10.1007/s11430-021-9868-9>.
- Pan, J., Bai, M., Li, C., Liu, F., Li, H., Liu, D., ... & Li, C. (2021). Coseismic surface rupture and seismogenic structure of the 2021-05-22 Maduo (Qinghai) MS 7.4 earthquake. *Acta Geologica Sinica*, 1655-1670. <https://doi.org/10.19762/j.cnki.dizhixuebao.2021166>.

- Accepted Article
- Stark, P. B., & Parker, R. L. (1995). Bounded-variable least-squares: an algorithm and applications. *Computational Statistics*, 10, 129-129.
- Scholz, C. H. (1998). Earthquakes and friction laws. *Nature*, 391(6662), 37–42. <https://doi.org/10.1038/34097>.
- Sreejith, K. M., Sunil, P. S., Agrawal, R., Saji, A. P., Ramesh, D. S., & Rajawat, A. S. (2016). Coseismic and early postseismic deformation due to the 25 April 2015, Mw 7.8 Gorkha, Nepal, earthquake from InSAR and GPS measurements. *Geophysical Research Letters*, 43(7), 3160-3168. <https://doi.org/10.1002/2016GL067907>.
- U. S. Geological Survey (USGS), 2021. Earthquake catalog released by U. S. Geological Survey. Available from: <https://earthquake.usgs.gov/earthquakes/eventpage/us7000e54r/finite-fault>, Accessed date: 21 May 2021.
- Van Der Woerd, J., Ryerson, F. J., Tapponnier, P., Gaudemer, Y., Finkel, R., Mériaux, A. S., ... & Qunlu, H. (1998). Holocene left-slip rate determined by cosmogenic surface dating on the Xidatan segment of the Kunlun fault (Qinghai, China). *Geology*, 26(8), 695-698. [https://doi.org/10.1130/0091-7613\(1998\)026<0695:HLSRDB>2.3.CO;2](https://doi.org/10.1130/0091-7613(1998)026<0695:HLSRDB>2.3.CO;2).
- Van Der Woerd, J., Tapponnier, P., J. Ryerson, F., Meriaux, A. S., Meyer, B., Gaudemer, Y., ... & Zhiqin, X. (2002). Uniform postglacial slip-rate along the central 600 km of the Kunlun Fault (Tibet), from ²⁶Al, ¹⁰Be, and ¹⁴C dating of riser offsets, and climatic origin of the regional morphology. *Geophysical Journal International*, 148(3), 356-388. <https://doi.org/10.1046/j.1365-246x.2002.01556.x>.
- Wells, D. L., & Coppersmith, K. J. (1994). New empirical relationships among magnitude, rupture length, rupture width, rupture area, and surface displacement. *Bulletin of the seismological Society of America*, 84(4), 974-1002.
- Wen, X., Yi, G., & Xu, X. (2007). Background and precursory seismicities along and surrounding the Kunlun fault before the Ms8. 1, 2001, Kokoxili earthquake, China. *Journal of Asian Earth Sciences*, 30(1), 63-72. <https://doi.org/10.1016/j.jseaes.2006.07.008>.
- Wen, Y., Li, Z., Xu, C., Ryder, I., & Bürgmann, R. (2012). Postseismic motion after the 2001 Mw 7.8 Kokoxili earthquake in Tibet observed by InSAR time series. *Journal of geophysical research: solid earth*, 117(B8). <https://doi.org/10.1029/2011JB009043>.
- Wessel, P., Smith, W. H., Scharroo, R., Luis, J., & Wobbe, F. (2013). Generic mapping tools: improved version released. *Eos, Transactions American Geophysical Union*, 94(45), 409-410.
- Wang, Y., Wang, M., & Shen, Z. K. (2017). Block-like versus distributed crustal deformation around the northeastern Tibetan plateau. *Journal of Asian Earth Sciences*, 140, 31-47. <https://doi.org/10.1016/j.jseaes.2017.02.040>.
- Wang, M., & Shen, Z. K. (2020). Present - day crustal deformation of continental China derived from GPS and its tectonic implications. *Journal of Geophysical Research: Solid Earth*, 125(2), e2019JB018774. <https://doi.org/10.1029/2019JB018774>.
- Wang, W., Fang, L., Wu, J., Tu, H., Chen, L., Lai, G., & Zhang, L. (2021). Aftershock sequence relocation of the 2021 MS7.4 Maduo Earthquake, Qinghai, China. *Science China Earth Sciences*, 1-10. <https://doi.org/10.1007/s11430-021-9803-3>.
- Zhang, G., Shan, X., & Feng, G. (2016). The 3-D surface deformation, coseismic fault slip and after-slip of the 2010

-
- Mw6.9 Yushu earthquake, Tibet, China. *Journal of Asian Earth Sciences*, 124, 260-268. <https://doi.org/10.1016/j.jseaes.2016.05.011>.
- Zheng, A., Chen, X., & Xu, W. (2020). Present-day deformation mechanism of the northeastern Minna deflection revealed by the 2020 Mw 6.5 Monte Cristo Range earthquake. *Geophysical Research Letters*, 47(22), e2020GL090142. <https://doi.org/10.1029/2020GL090142>.
- Zhu, Y., Diao, F., Fu, Y., Liu, C., & Xiong, X. (2021). Slip rate of the seismogenic fault of the 2021 Maduo earthquake in western China inferred from GPS observations. *Science China Earth Sciences*, 1-8. <https://doi.org/10.1007/s11430-021-9808-0>.
- Zhu, L., Ji, L., & Liu, C. (2021). Interseismic slip rate and locking along the Maqin–Maqu Segment of the East Kunlun Fault, Northern Tibetan Plateau, based on Sentinel-1 images. *Journal of Asian Earth Sciences*, 211, 104703. <https://doi.org/10.1016/j.jseaes.2021.104703>.
- Zhao, D., Qu, C., Chen, H., Shan, X., Song, X., & Gong, W. (2021). Tectonic and geometric control on fault kinematics of the 2021 Mw7.3 Maduo (China) earthquake inferred from interseismic, coseismic and postseismic InSAR observations. *Geophysical Research Letters*, e2021GL095417. <https://doi.org/10.1029/2021GL095417>.